(Received 16 January 2026, Accepted 15 February 2026, Scheduled 4 March 2026)

High Gain Circularly Polarized Dual-Band Antenna Array Using Hybrid Couplers

Qurratul Ayn[1, *], Yuvaraj Sivasubramanian[2], and Kiran K. Gurrala[1]

[1] *National Institute of Technology, Tadepalligudem, Andhra Pradesh, India*
[2] *IIITDM, Kancheepuram, Tamilnadu, India*

ABSTRACT: This work presents a dual-band circularly polarized antenna array in which adjacent elements are excited with quadrature phase progression using a cascaded hybrid-coupler feeding network comprising one rat-race coupler and two branch-line couplers. Double-T monopole elements enable dual-band operation, achieving impedance bandwidths of 300 MHz (2.4–2.7 GHz) and 975 MHz (5.025–6 GHz) with corresponding axial-ratio bandwidths of 110 MHz and 525 MHz. The array provides peak realized gains of 9.19 dBic and 9.49 dBic with simulated total efficiencies of 90% and 87% in the respective bands. Unlike sequential rotation or multilayer CP arrays, the proposed single-layer planar hybrid-coupler network ensures frequency-stable dual-band circular polarization. An analytical formulation of the array factor and axial ratio sensitivity is provided to clarify the CP synthesis mechanism and its suitability for compact vehicular platforms.

1. INTRODUCTION

Vehicular communication channels face highly dynamic propagation conditions in terms of multipath propagation, dynamic arrival angles, and Doppler shifts due to vehicular movements. In addition, reflections of the signal from surfaces of roads, adjacent vehicles, and surrounding structures can affect polarization, leading to poor quality in the antenna link. Circularly polarized antennae help to reduce these adverse effects by minimizing antenna orientation issues and polarization rotation. As a result, circularly polarized (CP) antennas are well-suited for WLAN and V2X vehicular communication systems.

These requirements motivate the development of compact, wideband, and polarization-stable dual-band CP antenna arrays capable of reliable operation in practical vehicular environments. In a single radiating element, CP is obtained by exciting two orthogonal modes with equal amplitude and a 90° phase difference, while in antenna arrays, CP can be synthesized through controlled phase progression between adjacent elements using techniques such as sequential rotation or radial stubs [15].

Several CP array configurations have been reported. Dual-band CP arrays using patches of different dimensions with cross-diagonal slots and sequential rotation are presented in [1], while tunable tri-band CP arrays employing varactor diodes and capacitance detuning are reported in [2]. Sequential-phase-fed single-band CP arrays are discussed in [3], whereas a dual-band array without CP operation using differential and series feeding is described in [4]. CP generation using orthogonal currents on dual-fed patches with phase compensation is demonstrated in [5], and shared-aperture dual-band CP arrays based on stacked and perforated patches are reported in [6]. A single-band phased CP array employing concentric circular loop elements is presented in [7]. The fundamental principles of array-factor formulation and phase-controlled excitation governing CP array performance are well established [22]. Recent studies have investigated circularly polarized antenna arrays using optimization techniques and advanced phase-control methods [23–25].

The 2.4 GHz band (2.4–2.4835 GHz) supports WLAN and Bluetooth applications, while the 5.2–5.9 GHz band is allocated for vehicle-to-everything (V2X) communications, making dual-band CP antennas suitable for intelligent transport systems, smart cities, industrial internet of things (IoT), unmanned aerial vehicles (UAVs), public safety, and defense applications. Recent advancements in array feeding networks include digitally controlled phase shifters [16] and Butler matrix-based multibeam systems [17], which provide accurate phase control but are more complex and bulky. Metasurface-assisted CP arrays [18] and reconfigurable designs using PIN diodes or varactors [19] provide polarization agility but require biasing networks and complex fabrication, while substrate-integrated waveguide (SIW) feeding networks, although low loss, are less suitable for low-cost FR4-based dual-band vehicular platforms.

Most reported dual-band circularly polarized (CP) arrays rely on geometric sequential rotation, multilayer structures, or frequency-selective phase networks, which increase fabrication complexity and limit phase stability across bands. This work addresses this gap by demonstrating frequency-stable dual-band CP synthesis using a single-layer cascaded hybrid-coupler feeding network, achieving quadrature phase excitation at both 2.4 GHz and 5.2 GHz without geometric rotation or multilayer implementation. Furthermore, analytical modelling of the array factor, axial-ratio sensitivity, and phase imbalance is presented to provide theoretical insight into the proposed dual-band CP

* Corresponding author: Qurratul Ayn (qurratulayn3@gmail.com).

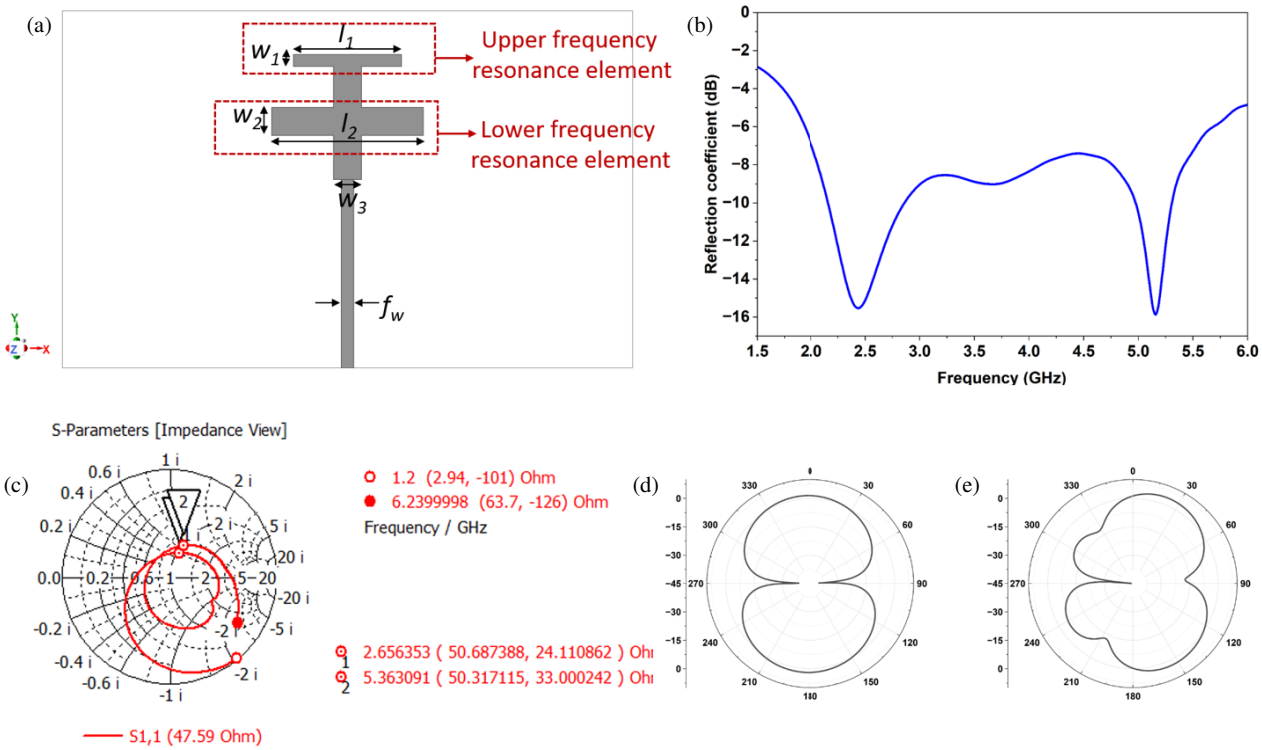

FIGURE 1. (a) Double-T monopole antenna, (b) its simulated reflection coefficient response, (c) Smith chart showing impedance matching for the dual operating bands, radiation patterns of dual T monopole at (d) 2.4 GHz and (e) 5.2 GHz.

mechanism and its applicability to compact vehicular antenna platforms [21].

2. ANTENNA DESIGN

2.1. Design of a Dual-Band Radiating Element Using a Double-T Monopole

In the first step, a dual-band radiating element based on a double-T monopole configuration, shown in Fig. 1(a), is designed and simulated using HFSS v2024. The antenna is implemented on a 1.6-mm-thick FR4 substrate with dielectric constant $\varepsilon_r = 4.3$ and loss tangent $\tan\delta = 0.02$, backed by a full ground plane. The radiating element is a combination of two T-shaped arms on a single monopole, allowing dual-band operation.

The dual-band operation is due to the two independent resonating current paths for the upper and lower T-arms. Each T-arm can be approximated as a quarter-wavelength monopole resonator, with the resonant frequency given by

$$f_i \approx \frac{c}{4L_{eff,i}\sqrt{\varepsilon_{eff}}}, \quad i = 1, 2 \tag{1}$$

where $L_{eff,i}$ is the effective electrical length of the ith T-arm, including fringing fields; ε_{eff} is the effective dielectric constant; and c is the speed of light. In the proposed antenna, the length of the lower T-arm, l_2, is mainly responsible for the resonance at the lower band of 2.4 GHz, and the length of the upper T-arm, l_1, is mainly responsible for the resonance at the upper band of 5.2 GHz.

The widths of the arms (w_1, w_2, w_3) and the feed width (f_w) have a secondary role in this case, as they affect impedance matching and bandwidth by adjusting the surface current distribution. A sequential parametric optimization was carried out in High Frequency Structure Simulator (HFSS), wherein l_1 and l_2 were first tuned to align the two resonant frequencies with the target bands, followed by the fine adjustment of widths to achieve -10 dB impedance matching. This allows for the minimization of mutual dependence between the two resonant modes. The optimization of the antenna design yields optimal values of $l_1 = 19$ mm, $l_2 = 30.5$ mm, $w_1 = 2.5$ mm, $w_2 = 2.9$ mm, $w_3 = 13.9$ mm, and $f_w = 9$ mm.

The Smith chart in Fig. 1(c) proves the stability of the input impedance as it remains close to the 50 Ω point for both 2.4 GHz and 5.2 GHz, showing good mutual impedance matching without spurious resonance. In order to validate the intrinsic properties of the designed antenna before the incorporation of the antenna array, the simulated properties of the isolated double-T monopole are given in Fig. 1. From these figures, the -10 dB impedance bandwidths of the antenna fully encompass the dual bands; the antenna also operates efficiently with considerable realized gains of approximately 3.1 dBi at 2.4 GHz and 3.4 dBi at 5.2 GHz. Figs. 1(d) and 1(e) present the radiation patterns that are relatively stable in terms of broadside radiation with monopole-like characteristics and good symmetry in both principal planes.

Note that the above gain values correspond to the isolated element. In the array environment, the effective element gain increases owing to mutual coupling and ground-plane effects

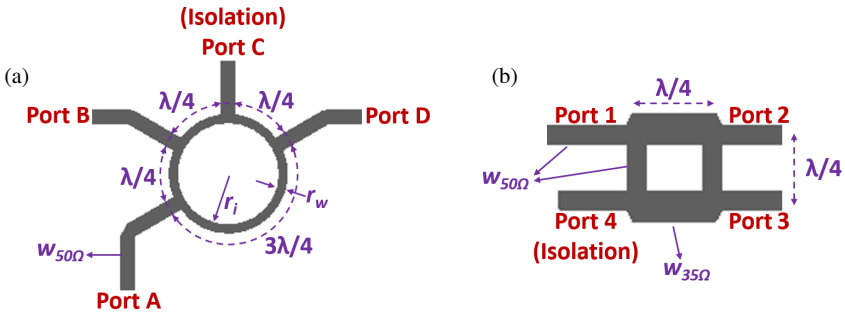

FIGURE 2. (a) Ring hybrid coupler and (b) quadrature hybrid coupler.

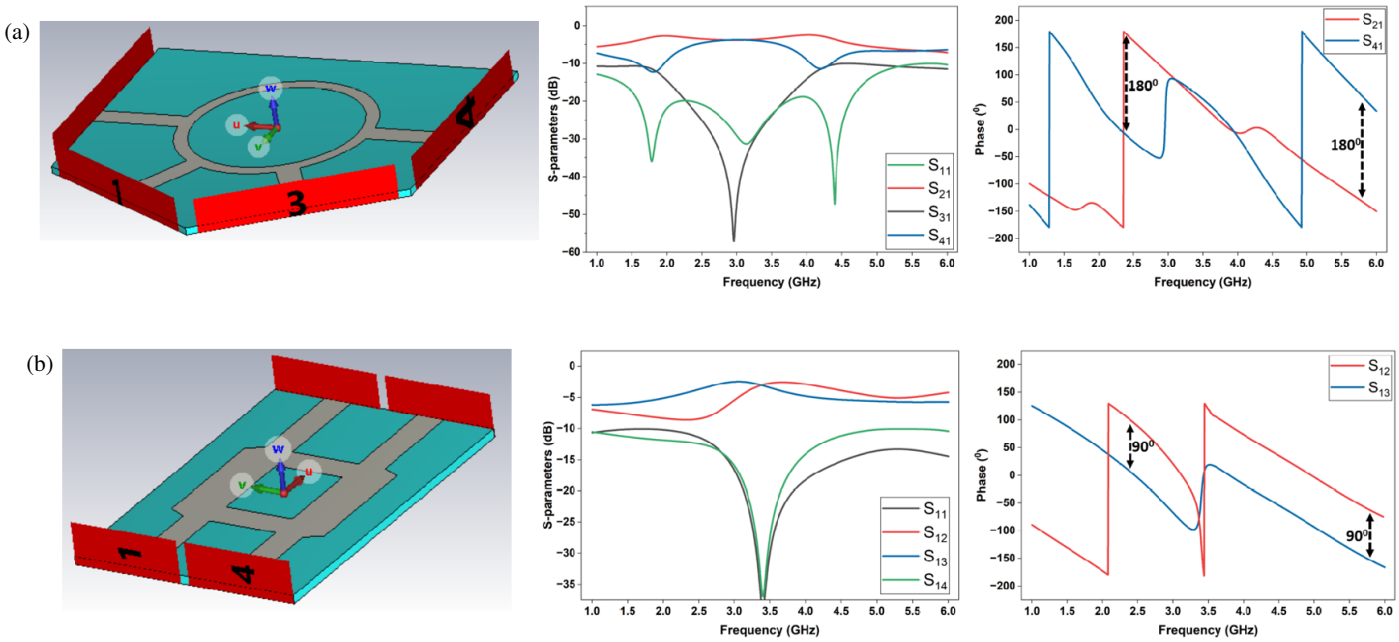

FIGURE 3. Simulated S-parameters response and phase vs frequency response of (a) ring coupler and (b) quadrature coupler.

that lead to a higher overall array gain in conjunction with the array factor. Based on these results, it can be concluded that the proposed radiating element provides sufficient bandwidth, gain, and radiation characteristics and serves as an adequate building block for the proposed circularly polarized antenna array.

2.2. Hybrid Couplers for Power Division and Phase Control

Power dividers and directional couplers are widely employed in antenna feeding networks to achieve equal power division and controlled phase delays, which are essential for synthesizing circular polarization (CP). CP radiation needs the excitation of two orthogonal modes with the same amplitude and a 90° phase difference. Quadrature hybrids or branch-line couplers act as 90° hybrids, offering equal 3 dB power splitting with a quadrature phase difference between the output ports, and are thus widely used for exciting orthogonal modes of antennas.

On the other hand, 180° hybrids, such as rat-race couplers, provide outputs with a 180° phase difference. By adding extra transmission line segments or cascaded feeding networks, rat-race couplers can be efficiently used for implementing quadrature phase progression, with satisfactory phase equality, port isolation, and polarization purity in antenna arrays and multi-band microwave networks.

In a ring hybrid coupler shown in Fig. 2(a), isolating port D and exciting port B generates two equal in-phase outputs at ports A and C, while isolating port C and exciting port A generates two equal outputs at ports B and D with a 180° phase difference. A rat-race coupler with isolated port C, as depicted in Fig. 3(a), is designed and analyzed using Computer Simulation Technology (CST) Microwave Studio. The coupler has an inner ring radius of $r_i = 8.68$ mm and a ring width of $r_w = 1.36$ mm.

The S-parameters in Fig. 3(a) show that the isolation between the isolated ports is greater than -20 dB over the 2.4 GHz band and greater than -10 dB over the 5.2 GHz band, ensuring that there is no unwanted coupling in the feeding network. When port 1 is excited as the input, the output magnitudes at ports 2 and 4 are almost equal, and the phase difference between them is about 180° over both frequency bands. The phase difference variation is within $\pm 5°$, ensuring that the out-of-phase excitation is consistent and adequate for dual-band sequential feeding.

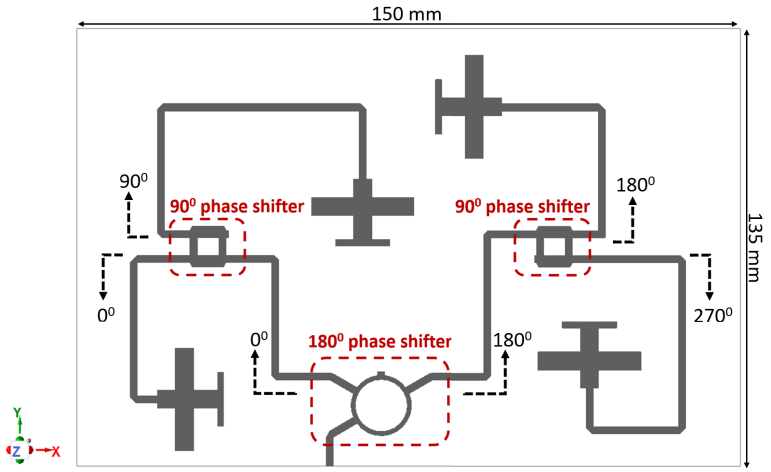

FIGURE 4. Top view of the proposed dual-band CP antenna array.

A quadrature hybrid coupler, as shown in Fig. 2(b), offers two equal-amplitude signals with a 90° phase shift, and the port on the same side as the input is isolated. A branch-line coupler with isolated port 4, as shown in Fig. 3(b), is designed and simulated using CST. The four arms are implemented using 50 Ω transmission lines, and the junction parts are implemented using 35 Ω transmission lines. The corresponding widths are $w_{50\Omega} = 2.35$ mm and $w_{35\Omega} = 3.82$ mm.

Figure 3(b) shows that, with port 1 as the input, the signals at ports 2 and 3 exhibit equal amplitudes and maintain a quadrature phase difference across the intended frequency bands. The branch-line couplers achieve simulated isolation better than 18 dB at 2.4 GHz and 20 dB at 5.2 GHz, ensuring stable quadrature phase excitation when being cascaded with the rat-race coupler in the proposed dual-band feeding network.

2.3. Proposed Dual-Band CP Antenna Array

The configuration of the proposed circularly polarized (CP) antenna array is shown in Fig. 4. The array is implemented on an FR4 substrate of thickness 1.6 mm, relative permittivity $\varepsilon_r = 4.3$, and loss tangent $\tan\delta = 0.02$. Both the radiating patches and the ground plane are fabricated using standard 0.035 mm thick copper cladding.

The corporate feeding network is realized using microstrip lines on the same FR4 substrate, with all transmission-line widths and electrical lengths explicitly defined to ensure design reproducibility. Optimized junctions, bends, and symmetric routing are utilized to minimize impedance discontinuities and phase errors. To take care of microstrip dispersion effects, the physical length of the transmission lines is adjusted in such a way that the necessary phase progression of 0°, 90°, 180°, and 270° is achieved over both bands. The spacing between elements is selected as $0.45\lambda_0$, which is a trade-off between mutual coupling reduction and grating lobe suppression. Even though a larger footprint is required to implement a corporate hybrid coupler network compared to series-fed or sequential rotation configurations, it exhibits better phase accuracy and dual-frequency CP performance.

The proposed feeding network is manifested in a cascaded form, consisting of a rat-race coupler followed by two branch-line couplers. The rat-race coupler splits power into two signals, having half amplitude, while achieving a 180° phase difference. These two signals are then supplied to branch-line couplers, which again split power into two parts, having half amplitude, but with a ±90° phase difference. This ensures a total of four output signals, having equal amplitude, and a sequential phase progression, thus allowing CP synthesis through the excitation of array elements, having a 180° phase separation between clusters, and a 90° phase separation within each cluster.

Figure 5 demonstrates the surface currents for different phases of excitation using the two frequencies, and the surface currents are shown to rotate clockwise with a phase difference of approximately 90°, which verifies the physical principle of producing circular polarization. Additional verification is achieved by analyzing the surface currents at four distinct phases, such as $\phi = 0°$, 90°, 180°, and 270°, with the locations of the maximum amplitude rotating and completing a circle of 360° within the period of excitation. These observations verify the successful generation of sequential phase excitations using the proposed hybrid coupler feed network and the stable operation of dual-band circular polarization.

2.4. Theoretical Analysis of Dual-Band Sequentially Phased Circularly Polarized Array

Although circular polarization can be synthesized in multi-antenna arrays using sequential phase excitation, achieving frequency-stable dual-band circular polarization through conventional geometric sequential rotation alone is challenging, due to the strong frequency dependence of phase balance and polarization purity. This section describes a unified analytical approach to understanding how a cascaded hybrid coupler structure supports stable quadrature phase progression and dual-band CP operation.

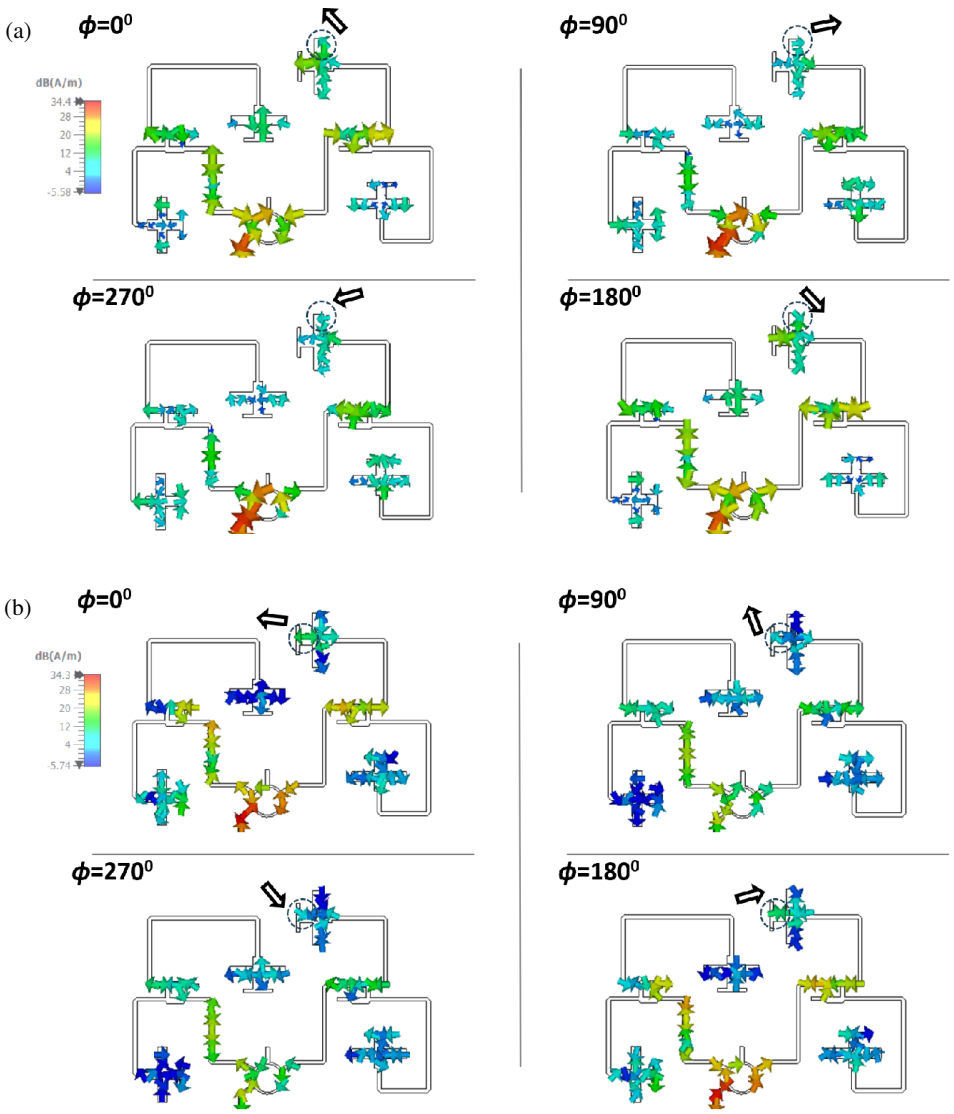

FIGURE 5. Simulated vector surface current distribution for different phase instances at frequencies: (a) 2.4 GHz and (b) 5.2 GHz.

2.4.1. Array Factor with Sequential Phase Progression

Let us consider a uniform four-element linear array placed along the x-axis with a spacing of d between elements. The array factor (AF) is given by

$$\mathrm{AF}(\theta) = \sum_{n=0}^{3} a_n e^{j(nkd\sin\theta+\phi_n)} \tag{2}$$

where a_n and ϕ_n represent the excitation amplitude and phase of the nth element, respectively; $k = 2\pi/\lambda$ is the wave number; and θ is the observation angle.

For the proposed sequential feeding network:

$$a_n = a_0, \quad \phi_n = n \times 90^\circ \tag{3}$$

Substituting these values yields

$$\mathrm{AF}(\theta) = a_0 \sum_{n=0}^{3} e^{jn(kd\sin\theta+\frac{\pi}{2})} \tag{4}$$

At boresight ($\theta = 0$), the spatial phase term is zero, and the excitation phase progression is strictly temporal. Under this scenario, the orthogonal field components constructively combine, facilitating circular polarization at the array output.

2.4.2. Mechanism of Circular Polarization Generation

Each double-T monopole array element radiates a linearly polarized field; therefore, circular polarization (CP) is achieved through far-field superposition. In the proposed array, equal-amplitude excitations with a sequential phase progression of 0°, 90°, 180°, and 270° are offered by the cascaded hybrid-coupler network.

The sequential phase excitation results in two orthogonal transverse electric-field components of equal amplitude with a $\pm 90^\circ$ phase difference at boresight, producing

$$E(t) = E_0\left(\hat{x}\cos(\omega t) + \hat{y}\sin(\omega t)\right) \tag{5}$$

which corresponds to a circularly polarized wave. This technique, also known as sequential phase CP synthesis, has long

been known for linearly polarized element arrays and has been extensively treated in [26]. The obtained CP performance is verified by the axial ratio results in Section 3.

2.4.3. Axial Ratio Formulation and Sensitivity Analysis

The axial ratio (AR), which is the ratio of the major to minor axes of the polarization ellipse, can be written as

$$\mathrm{AR} = \frac{|E_{\max}|}{|E_{\min}|} \tag{6}$$

For two orthogonal field components E_x and E_y with amplitude ratio $\alpha = |E_y|/|E_x|$ and phase difference $\Delta\phi$, the AR can be approximated as

$$\mathrm{AR} = \sqrt{\frac{1+\alpha^2+2\alpha\cos(\Delta\phi)}{1+\alpha^2-2\alpha\cos(\Delta\phi)}} \tag{7}$$

Ideal CP is achieved when $\alpha = 1$ and $\Delta\phi = 90°$. Violations of these assumptions lead to a degradation of the AR, thus emphasizing the need for precise phase control and equal power splitting, which are naturally ensured by the rat-race and branch-line hybrid couplers employed in the proposed feed network.

2.4.4. Effect of Phase and Amplitude Errors

In practical circularly polarized antenna arrays, small amplitude and phase imbalances introduced by the feeding network directly affect the achievable axial ratio (AR). Let the normalized amplitude ratio between two orthogonal field components be $\alpha = 1+\delta$ and the phase difference be $\Delta\phi = 90° + \varepsilon$, where δ denotes the amplitude imbalance, and ε represents the phase error.

Substituting these quantities into the general AR expression and applying a first-order Taylor expansion about $\delta = 0$ and $\varepsilon = 0$ yields the intermediate approximation

$$\mathrm{AR} \approx \sqrt{(1-\alpha)^2 + (\Delta\phi - 90°)^2} \tag{8}$$

Expressed in terms of the perturbation variables, it is simplified to

$$\mathrm{AR} \approx \sqrt{\delta^2 + \epsilon^2} \tag{9}$$

where AR is in linear scale, and ε is expressed in radians. This approximation is valid for very small perturbations, typically $|\delta| < 0.1$ and $|\varepsilon| < 10°$.

For the proposed cascaded hybrid-coupler network, simulations indicate an amplitude imbalance within ± 0.5 dB ($\delta \approx 0.06$) and a phase deviation within $\pm 5°$ ($\varepsilon \approx 0.087$ rad). Substituting these values predicts AR ≈ 1.05 (≈ 0.4 dB), which closely matches the simulated minimum axial ratio near boresight. This agreement confirms that the proposed feeding network provides stable circular polarization and is tolerant to realistic amplitude and phase errors.

2.4.5. Mutual Coupling Considerations

The mutual coupling between the array elements usually has an effect on the input matching and excitation phase, which, in certain instances, might have an adverse effect on the purity of the CP signal. In the proposed array, the distance between the array elements has been optimized, considering the trade-off between the coupling suppression and the array size itself. In this context, the mutual coupling effect was taken care of using the mutual impedance matrix given by $[Z]$; the diagonal elements of this matrix account for the self-impedance, and the off-diagonal elements account for the mutual coupling between the array elements.

From HFSS simulations, the self-impedance at 2.4 GHz is approximately $Z_{11} \approx (42 + \mathrm{j}18)\,\Omega$, with nearest-neighbour coupling $Z_{12} \approx (6 - \mathrm{j}9)\,\Omega$. At 5.2 GHz, these values become $Z_{11} \approx (48 + \mathrm{j}22)\,\Omega$ and $Z_{12} \approx (4 - \mathrm{j}7)\,\Omega$. Port-based impedance extraction was implemented to extract these impedances from full-wave simulations, with all other ports terminated in 50 Ω. The significantly lower magnitude of mutual impedance confirms weak-to-moderate coupling, resulting in only minor perturbations to impedance matching and axial ratio. The symmetric feed network and equal electrical path lengths further suppress coupling-induced phase errors, preserving the intended sequential excitation. A full mutual impedance matrix analysis is beyond the scope of this application-oriented study and is left for future work.

2.4.6. Relevance to Dual-Band Operation

Unlike conventional sequential-rotation techniques based on geometrical patch rotation, the proposed array achieves circular polarization through frequency-stable electrical phase control. The cascaded hybrid-coupler network maintains consistent quadrature phase relationships at both 2.4 GHz and 5.2 GHz, enabling simultaneous dual-band CP operation using a single planar feed topology.

3. RESULTS AND OBSERVATIONS

The dual-band circularly polarized antenna array for vehicular communication is designed and optimized using HFSS v2024. A prototype is developed, and experimental verification

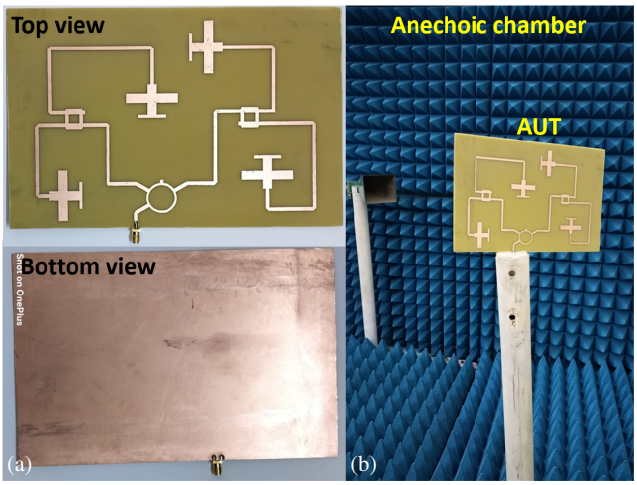

FIGURE 6. (a) Fabricated prototype of proposed antenna array and (b) measurement setup.

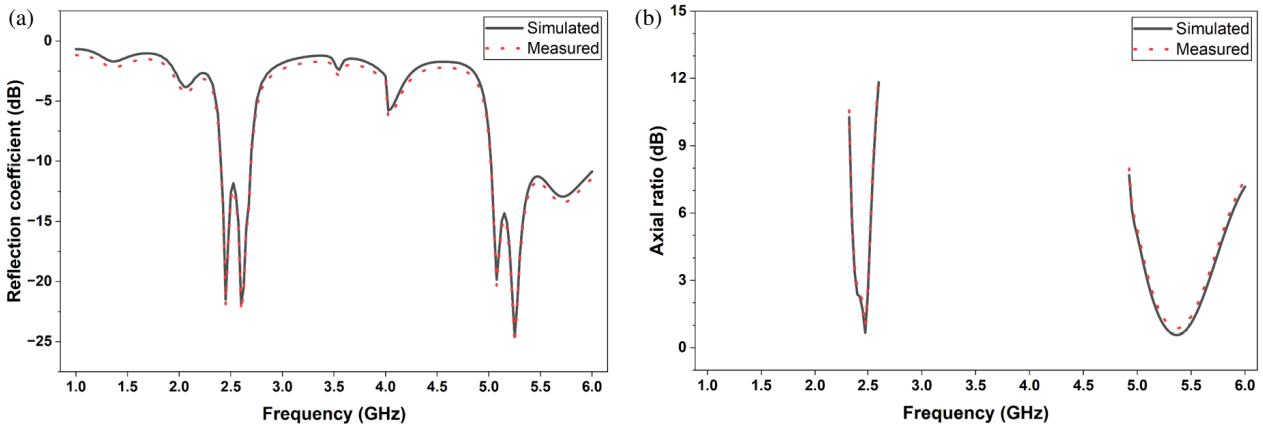

FIGURE 7. (a) Reflection coefficient vs frequency plot and (b) axial ratio vs frequency plot.

is carried out by reflection and radiation pattern measurements. Fig. 6 shows the fabricated antenna and measurement setup. The performance of the array is tested in terms of impedance and axial ratio bandwidths, maximum gain, and radiation efficiency over the two frequency bands. The measurement results match well with the simulation ones.

The results of all measurements contain uncertainties due to the instrumentation, calibration, and environmental conditions. The uncertainty in reflection coefficient measurements using a calibrated vector network analyzer is within ± 0.15 dB. The radiation pattern and gain measurements in an anechoic chamber have an overall uncertainty of about ± 0.5 dB, primarily due to the alignment errors, cable losses, and the calibration of the reference antenna. The uncertainty in axial ratio measurements is affected by the polarization alignment and chamber reflections, and it is about ± 0.3 dB near the boresight direction. To reduce the uncertainties, multiple measurements were averaged, and the presented impedance bandwidth, axial ratio bandwidth, and gain values are accurate within the specified uncertainty limits.

3.1. Reflection Coefficient and Axial Ratio

Figure 7 shows the measured reflection coefficient and axial-ratio responses of the proposed dual-band CP array over the 1–6 GHz range. The -10 dB impedance bandwidths are 300 MHz (2.4–2.7 GHz) and 975 MHz (5.025–6 GHz), while the corresponding 3 dB axial-ratio bandwidths are 110 MHz (2.4–2.51 GHz) and 525 MHz (5.125–5.65 GHz). The broader axial-ratio bandwidth at the higher band is attributed to improved phase balance of the hybrid-coupler network and electrically smaller radiating elements, which produce more stable orthogonal field components. In contrast, the lower band exhibits reduced axial-ratio bandwidth due to the increased electrical size of the elements and higher sensitivity to phase and impedance variations.

To assess angular polarization stability, the 3-dB axial-ratio beamwidth (ARBW) is extracted from the simulated axial-ratio radiation patterns shown in Fig. 8. At 2.4 GHz, the array maintains AR $\leq$ 3 dB over approximately $\pm 25^\circ$ in the E-plane and $\pm 33^\circ$ in the H-plane around boresight, while at 5.2 GHz, the corresponding ARBW extends to approximately

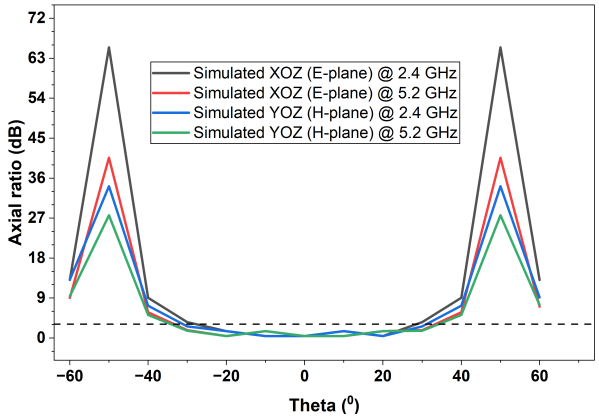

FIGURE 8. Simulated AR radiation patterns of the proposed antenna array at 2.4 GHz and 5.2 GHz, showing the angular variation of $\phi = 0^\circ$ and $\phi = 90^\circ$ over the visible hemisphere.

$\pm 30^\circ$ and $\pm 35^\circ$, respectively. Due to practical limitations of the available measurement setup in accurately characterizing angular AR with phase-resolved orthogonal field components, AR-versus-angle results are reported from full-wave simulations. The experimental validation of circular polarization is therefore provided through frequency-domain AR measurements and radiation-pattern measurements, which exhibit good agreement with simulations. These results confirm stable angular CP performance within the main beam, suitable for vehicular communication environments.

3.2. Gain and Efficiency

The proposed CP antenna array exhibits peak realized gains of 9.19 dBic in the WLAN/Wi-MAX band and 9.49 dBic in the vehicular communication band. The corresponding 3D gain radiation patterns are shown in Fig. 9. When being integrated into the four-element array, the effective embedded element gain increases due to mutual coupling, finite ground-plane diffraction, and current redistribution among adjacent elements. Full-wave HFSS simulations indicate embedded element gains of approximately 3.1 dBi at 2.4 GHz and 3.4 dBi at 5.2 GHz. For a four-element array, the array-factor contribution

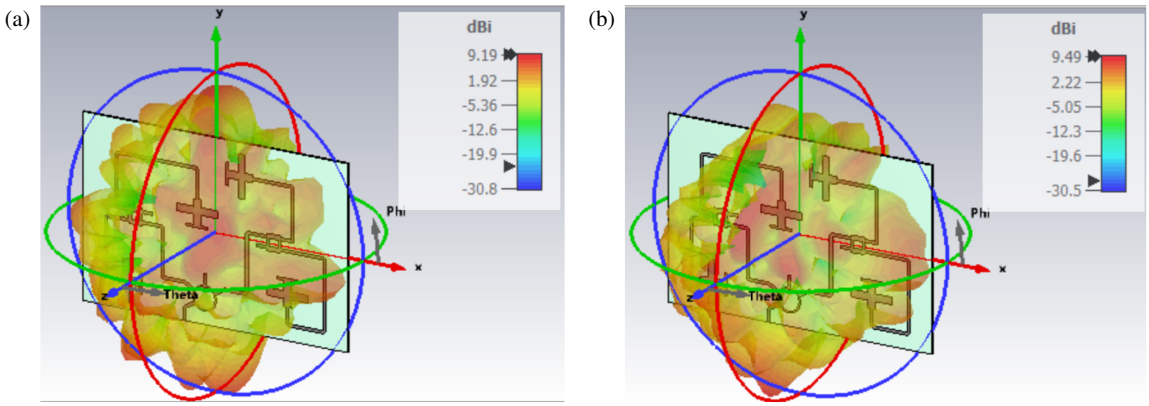

FIGURE 9. Peak realized gain at 2.4 GHz and 5.2 GHz.

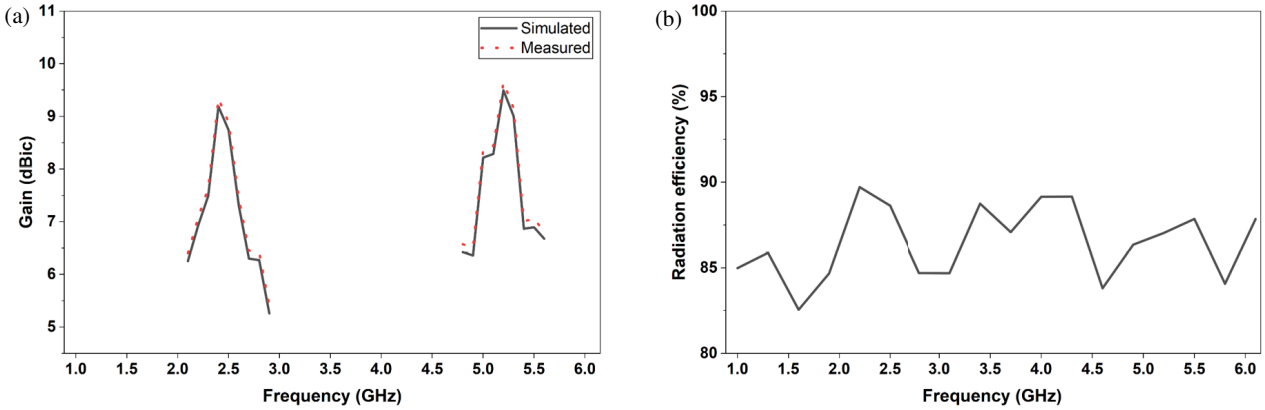

FIGURE 10. Axial ratio and gain vs frequency plots.

of $10 \cdot \log_{10}(4) = 6.02$ dBic results in expected peak gains of approximately 9.1–9.2 dBic and 9.4–9.5 dBic in the lower and upper bands, respectively. The simulated peak realized gains of 9.19 dBic at 2.4 GHz and 9.49 dBic at 5.2 GHz are therefore consistent with array-gain theory.

Figure 10 shows the gain and efficiency of the array as a function of frequency. The array has a constant gain in both frequency bands and a simulated total efficiency of about 90% at 2.4 GHz and 87% at 5.2 GHz, taking into account the conductor and dielectric losses in the FR4 substrate. The efficiency values were extracted from the full-wave simulation and were not directly measured, because of the limitations in the measurement setup. However, the good agreement between the simulated and measured gains and radiation patterns serves as an indirect verification of the simulated efficiency values. The mismatch losses are negligible, because of the good impedance matching, as verified by the measured $|S_{11}|$. The slight efficiency drop at 5.2 GHz is mainly due to the increased dielectric and conductor losses, which is in line with the frequency-dependent loss behavior of FR4 substrates.

The efficiency performance of the proposed array was also investigated by decomposing the radiation efficiency and mismatch loss using HFSS post-processing. For 2.4 GHz, the simulated radiation efficiency is about 84%, and for 5.2 GHz, it is about 81%, taking into account the conductor and dielectric losses only. However, when impedance mismatch is taken into account, the total efficiency (antenna efficiency) is found to be around 90% at 2.4 GHz and 87% at 5.2 GHz due to the excellent impedance matching in the respective bands.

3.3. Radiation Patterns

Figure 11 depicts the simulated and measured co- and cross-polarization patterns of the proposed antenna array design at 2.4 GHz and 5.2 GHz. As can be seen, in both bands, the measured patterns are in excellent agreement with the simulated ones, thus verifying the stable broadside radiation of the proposed design. The co-polarized components are found to be dominant, and the cross-polarized components are at least 15–20 dB lower in the main beam.

The cross-polarization discrimination (XPD), defined as the difference between right-hand CP (RHCP) and left-hand CP (LHCP) components at boresight, exceeds 18 dB at 2.4 GHz and 16 dB at 5.2 GHz, as shown in Fig. 11. Minor deviations in sidelobe levels between simulation and measurement are attributed to fabrication tolerances, FR4 dielectric constant variations, connector losses, and finite ground-plane effects.

The effect of the presence of higher-order modes and any unwanted radiation due to the feeding network has also been in-

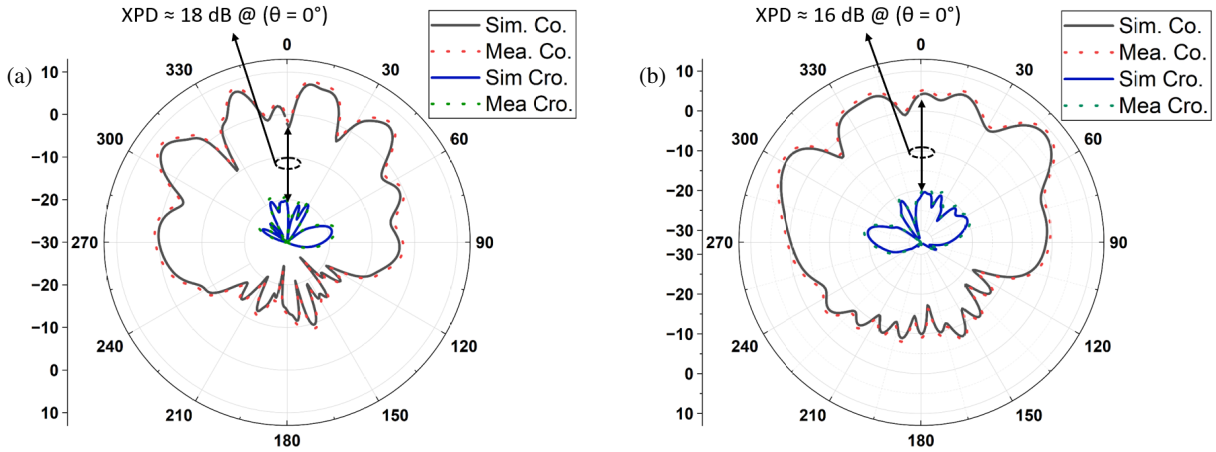

FIGURE 11. Simulated and measured co-polarized and cross-polarized radiation patterns of the proposed antenna array at (a) 2.4 GHz and (b) 5.2 GHz in the principal planes.

TABLE 1. Comparison with existing designs in the literature.

Ref.	Size (mm^3)	Impedance bandwidths (GHz)	Axial ratio bandwidths (GHz)	Peak realized gain (dBic)	Total efficiency (%)
[8]	45 × 45 × 1.524	2.18–2.50 (320 MHz) 5.33–9.06 (3730 MHz)	2.32–2.58 (260 MHz) 5.66–6.08 (420 MHz)	3.5 6.2	80 60
[9]	134.96 × 134.96 × 0.8	2.04–3.25 (1210 MHz) 5.37–7.38 (2010 MHz)	NA	2.97 6.49	96 89
[10]	40 × 40 × 1.6	2.396–2.525 (129 MHz) 4.91–5.38 (470 MHz)	2.29–2.67 (380 MHz) 5–5.08 (80 MHz)	5.01 5.27	NA
[11]	ND	2.258–2.571 (313 MHz) 3.978–5.887 (1909 MHz)	NA	3.24 7.09	65–75 55–65
[12]	120 × 50 × 0.6	2.25–2.63 (380 MHz) 5.14–6.06 (920 MHz)	NA	5.2 6.7	81 70.7
[13]	32 × 40 × 0.8	(200 MHz) (1500 MHz)	ND	7.5 7.8	NA
[14]	ND	2.13–2.5 (370 MHz) 4.56–7.05 (2490 MHz)	NA	8.65 10.27	NA
[20]	200 × 200 × 13	1.565–1.578 (13 MHz) 2.2–3.8 (1600 MHz) 5.8–6.0 (200 MHz)	CP in only 2nd operating band (at 3 GHz)	7 8.3 5.3	81 90 85
*This work	150 × 135 × 1.6	2.4–2.7 (300 MHz) 5.025–6 (975 MHz)	2.4–2.51 (110 MHz) 5.125–5.65 (525 MHz)	9.19 9.49	90 87

Note: NA — Not Available, ND — Not Disclosed

vestigated; the microstrip line indeed supports the quasi-TEM mode predominantly in both frequency bands, and the symmetric corporate feeding approach has been shown to suppress the imbalance in the currents and any unwanted radiation, which would have resulted in any pattern distortion and unwanted sidelobes, respectively. The finite ground plane mainly affects the level of back radiation and sidelobes. The direction of the main beam, peak gain, and performance of axial ratio remain largely the same, proving the stability of the radiation characteristics under real-world constraints of vehicular deployment.

3.4. Comparison with State-of-the-Art Designs

To highlight the contribution of the work presented, the proposed antenna array is compared with existing antennas with respect to the antenna's size, impedance bandwidth, axial ratio bandwidth, peak gain, and efficiency, as compiled in Table 1.

For the proposed array, the ratio of axial-ratio bandwidth to impedance bandwidth (ARBW/IBW) is approximately 0.37 at 2.4 GHz and 0.54 at 5.2 GHz. Based on the 1.6-mm FR4 substrate, the corresponding electrical thicknesses are $h/\lambda_0 \approx$

0.012 at 2.4 GHz and $h/\lambda_0 \approx 0.026$ at 5.2 GHz, which are comparable to or smaller than those of reported CP arrays in Table 1.

The arrays with higher efficiency or bandwidths tend to involve multilayer substrates or metasurface structures. These features naturally add complexity and expense to their fabrication. On the other hand, the proposed CP array presents an array of a single-layer substrate with a coplanar cascaded hybrid coupler, focusing instead on the polarization properties and dual-band consistency.

While the proposed array displays lower peak gain than other arrays with higher dimensions and numbers of elements, it is an intended trade-off for smaller dimensions, complexity, and ease of integration, all of which are significant factors for vehicular applications. The total conventional CP arrays may involve sequences of rotation and specific geometrical manipulations of the radiating elements. These features are very difficult for dual-band characteristics and often lead to multilayer stack structures. On the contrary, the suggested CP array comprises cascaded hybrid couplers for producing an electrically controlled circularly polarized array.

Compared with other multi-feed CP arrays using an external phase shifter, adaptive beam forming network, and Butler matrix, the designed architecture presents the advantages of compactness, robustness, and low system complexity at the expense of beam agility. In sharp contrast with series-fed dual-band arrays that often possess frequency-sensitive amplitude and phase imbalance, the corporate combining hybrid coupler ensures an equal division of power with high isolation and phase balance for the frequency bands. Optimized feeding techniques have been discussed in [23], whereas phase control-based circular polarization generation and beam steering techniques were discussed in [24] and [25]. However, these microstrip arrays lack considerations of frequency-stable dual-band circular polarization generation via a single-layer hybrid coupler feeding network. The research paper presents frequency-stable dual-band circular polarization generation via a single-layer hybrid coupler feeding network.

The overall balanced performance of this proposed dual-band CP array lies in its compromise on purity, gain, compactness, and low complexities. The cascaded hybrid-coupler feed maintains amplitude imbalance within ± 0.5 dB and phase error within $\pm 5°$, resulting in a wide axial-ratio bandwidth and stable beamwidth. Despite the use of a low-cost FR4, the array achieves total efficiencies of 90% and 87% with peak realized gains exceeding 9 dBic, confirming its suitability for compact WLAN and V2X vehicular applications.

4. CONCLUSION

A dual-band circularly polarized antenna array employing cascaded hybrid couplers for power division and phase control has been presented for vehicular communication applications. The array achieves -10 dB impedance bandwidths of 300 MHz (2.4–2.7 GHz) and 975 MHz (5.025–6 GHz), with corresponding axial-ratio bandwidths of 110 MHz (2.4–2.51 GHz) and 525 MHz (5.125–5.65 GHz). Peak realized gains of 9.19 dBic and 9.49 dBic are obtained in the lower and upper bands, respectively, with total efficiencies of approximately 90% and 87% at the two operating bands. The primary contribution of this work is the demonstration of frequency-stable dual-band circular polarization synthesis through electrical phase control using a single-layer hybrid-coupler feeding network, avoiding geometrical rotation or multilayer configurations. Although it is validated on a four-element array, the proposed cascaded hybrid-coupler architecture is inherently scalable and can be extended to larger arrays or beam-steerable and reconfigurable systems. The use of low-cost FR4 introduces higher dielectric losses at the upper band, representing a trade-off between efficiency and fabrication simplicity. Future work will focus on low-loss substrates and adaptive feeding networks to further enhance gain, bandwidth, and polarization purity.

REFERENCES

[1] Zhang, J.-D., W. Wu, and D.-G. Fang, "Dual-band and dual-circularly polarized shared-aperture array antennas with single-layer substrate," *IEEE Transactions on Antennas and Propagation*, Vol. 64, No. 1, 109–116, Jan. 2016.

[2] Ikram, M., N. Nguyen-Trong, and A. Abbosh, "A simple single-layered continuous frequency and polarization-reconfigurable patch antenna array," *IEEE Transactions on Antennas and Propagation*, Vol. 68, No. 6, 4991–4996, Jun. 2020.

[3] Siahcheshm, A., J. Nourinia, and C. Ghobadi, "Circularly polarized antenna array with a new sequential phase feed network utilizing directional coupler," *AEU — International Journal of Electronics and Communications*, Vol. 93, 75–82, 2018.

[4] Govindarajulu, S. R., R. Hokayem, M. N. A. Tarek, M. R. Guerra, and E. A. Alwan, "Low profile dual-band shared aperture array for vehicle-to-vehicle communication," *IEEE Access*, Vol. 9, 147 082–147 090, 2021.

[5] Liu, Y., K. Huang, and X. Luo, "Circularly polarized antenna array fed by air-bridge free CPW-slotline network," *International Journal of Antennas and Propagation*, Vol. 2017, No. 1, 5230142, 2017.

[6] Kim, J.-H., S. K. Hong, and B.-G. Kim, "A shared-aperture S/X dual broadband microstrip antenna with one perforated patch," *Microwave and Optical Technology Letters*, Vol. 62, No. 1, 507–513, 2020.

[7] Asfour, R. W., S. K. Khamas, and E. A. Ball, "Design and measurements of circularly polarized millimeter-wave phased array antenna using time delay transmission lines," *IEEE Access*, Vol. 11, 122 016–122 028, 2023.

[8] Deng, X., P. Yang, S. Chen, and W. Ren, "Design of a 2.4 & 5.8 GHz efficient circularly polarized rectenna for wireless power transfer applications," *Electronics*, Vol. 12, No. 12, 2645, 2023.

[9] Raza, M. U., H. Ren, and S. Yan, "Dual-band monopole MIMO antenna array for UAV communication systems," *Sensors*, Vol. 24, No. 18, 5913, 2024.

[10] Almehmadi, A. S. and R. W. Aldhaheri, "A novel design of dual-band circularly polarized microstrip patch antenna for unmanned aerial vehicle applications," *Applied Sciences*, Vol. 15, No. 4, 1816, 2025.

[11] Saputro, B. R., H. Ludiyati, K. Paramayudha, Vitrasia, and E. Mozef, "A planar omnidirectional microstrip antenna for 2.4 and 5.8 GHz telemetry in drone ground control stations," *E3S Web of Conferences*, Vol. 664, 04001, Nov. 2025.

[12] Zhang, W., Y. Li, K. Wei, and Z. Zhang, "A dual-band MIMO antenna system for 2.4/5 GHz WLAN applications," *IEEE Transactions on Antennas and Propagation*, Vol. 71, No. 7,

5749–5758, Jul. 2023.

[13] Kazemi, F., "Miniaturized array antenna base on metamaterial structures," *AEU — International Journal of Electronics and Communications*, Vol. 138, 153832, Aug. 2021.

[14] Ma, Z. L. and H. F. Peng, "A 2.4 GHz/5.8 GHz dual-band shared-aperture antenna for WiFi applications," in *2025 IEEE International Workshop on Electromagnetics: Applications and Student Innovation Competition (iWEM)*, 168–170, Hong Kong, 2025.

[15] Balanis, C. A., *Antenna Theory: Analysis and Design*, John Wiley & Sons, 2016.

[16] Adamidis, G. A., I. O. Vardiambasis, M. P. Ioannidou, and T. N. Kapetanakis, "Design and implementation of an adaptive beamformer for phased array antenna applications," *Microwave and Optical Technology Letters*, Vol. 62, No. 4, 1780–1784, 2020.

[17] Adamidis, G. A., I. O. Vardiambasis, M. P. Ioannidou, and T. N. Kapetanakis, "Design and implementation of single-layer 4×4 and 8×8 Butler matrices for multibeam antenna arrays," *International Journal of Antennas and Propagation*, Vol. 2019, No. 1, 1645281, 2019.

[18] Li, Z., Y. Liu, M. Zhao, W. Zong, and S. He, "A wideband circularly polarized metasurface antenna with high gain using characteristic mode analysis," *Electronics*, Vol. 14, No. 14, 2818, 2025.

[19] Chen, J.-Y. and J.-S. Row, "Reconfigurable circularly polarized antenna with frequency agility," *Microwave and Optical Technology Letters*, Vol. 64, No. 3, 559–564, 2022.

[20] Li, M., Y. Su, W. Zhang, and X. Lin, "A versatile shared-aperture antenna for vehicle communications," *Electronics*, Vol. 13, No. 20, 4009, 2024.

[21] Milligan, T. A., *Modern Antenna Design*, John Wiley & Sons, 2005.

[22] Hansen, R. C., *Phased Array Antennas*, John Wiley & Sons, 2009.

[23] Dhar, P. K., "Optimization of a circularly polarized conical beam microstrip patch antenna array conformed on a cylindrical surface using HFSS," *Progress In Electromagnetics Research C*, Vol. 130, 183–199, 2023.

[24] Pouhè, D., "A technique for alternating generation of single and multi-beams from circularly polarized antenna arrays," *Progress In Electromagnetics Research B*, Vol. 109, 69–80, 2024.

[25] Guo, X., M. Du, W. Wu, Z. Feng, and Z. Wan, "Circularly polarized antenna array using filtering phase shifting theory," *Progress In Electromagnetics Research Letters*, Vol. 116, 9–16, 2024.

[26] Huang, J. and R. J. Pogorzelski, "A Ka-band microstrip reflectarray with elements having variable rotation angles," *IEEE Transactions on Antennas and Propagation*, Vol. 46, No. 5, 650–656, May 1998.